The Astrophysical Journal Letters, 970:L20 (14pp), 2024 July 20 https://doi.org/10.3847/2041-8213/ad5d74
© 2024. The Author(s). Published by the American Astronomical Society.
OPEN ACCESS

Constraining Possible γ-Ray Burst Emission from GW230529 Using Swift-BAT and Fermi-GBM

Samuele Ronchini[1,2], Suman Bala[3], Joshua Wood[4], James Delaunay[1], Simone Dichiara[1], Jamie A. Kennea[1], Tyler Parsotan[5], Gayathri Raman[1], Aaron Tohuvavohu[6,7], Naresh Adhikari[8], Narayana P. Bhat[9], Sylvia Biscoveanu[10], Elisabetta Bissaldi[11,12], Eric Burns[13], Sergio Campana[14], Koustav Chandra[2], William H. Cleveland[3], Sarah Dalessi[15,16], Massimiliano De Pasquale[17], Juan García-Bellido[18], Claudio Gasbarra[19,20], Misty M. Giles[21], Ish Gupta[2], Dieter Hartmann[22], Boyan A. Hristov[16], Michelle C. Hui[4], Rahul Kashyap[2], Daniel Kocevski[4], Bagrat Mailyan[23], Christian Malacaria[24], Hiroyuki Nakano[25], Giacomo Principe[26,27,28], Oliver J. Roberts[29], Bangalore Sathyaprakash[2], Lijing Shao[30,31], Eleonora Troja[32,33], Péter Veres[9,34], and Colleen A. Wilson-Hodge[4]

[1] Department of Astronomy and Astrophysics, The Pennsylvania State University, 525 Davey Lab, University Park, PA 16802, USA
[2] Institute for Gravitation & the Cosmos, The Pennsylvania State University, University Park, PA 16802, USA
[3] Science and Technology Institute, Universities Space Research Association, Huntsville, AL 35805, USA
[4] NASA Marshall Space Flight Center, Huntsville, AL 35812, USA
[5] Astrophysics Science Division, NASA Goddard Space Flight Center, Greenbelt, MD 20771, USA
[6] Department of Astronomy & Astrophysics, University of Toronto, Toronto, ON M5S 3H4, Canada
[7] Dunlap Institute for Astronomy & Astrophysics, University of Toronto, Toronto, ON M5S 3H4, Canada
[8] Leonard E. Parker Center for Gravitation, Cosmology, and Astrophysics, University of Wisconsin–Milwaukee, Milwaukee, WI 53201, USA
[9] Center for Space Plasma and Aeronomic Research, University of Alabama in Huntsville, Huntsville, AL 35899, USA
[10] Center for Interdisciplinary Exploration and Research in Astrophysics (CIERA), Northwestern University, Evanston, IL 60201, USA
[11] Dipartimento Interateneo di Fisica, Politecnico di Bari, Via G. Amendola 173, 70125 Bari, Italy
[12] Istituto Nazionale di Fisica Nucleare, Sezione di Bari, Via E. Orabona 4, 70125 Bari, Italy
[13] Department of Physics & Astronomy, Louisiana State University, Baton Rouge, LA 70803, USA
[14] INAF-Osservatorio Astronomico di Brera, Via E. Bianchi 46, 23807 Merate, LC, Italy
[15] Department of Space Science, University of Alabama in Huntsville, 320 Sparkman Drive, Huntsville, AL 35899, USA
[16] Center for Space Plasma and Aeronomic Research, The University of Alabama in Huntsville, Huntsville, AL 35899, USA
[17] MIFT Department, Polo Papardo, University of Messina, Viale Ferdinando Stagno d'Alcontres, 31, 98166 Messina, Italy
[18] Instituto de Física Teórica UAM/CSIC, Universidad Autónoma de Madrid, Cantoblanco 28049 Madrid, Spain
[19] Dipartimento di Fisica, Università di Roma Tor Vergata, I-00133 Roma, Italy
[20] Istituto Nazionale di Fisica Nucleare, Sezione di Roma Tor Vergata, I-00133 Roma, Italy
[21] Jacobs Space Exploration Group, Huntsville, AL 35806, USA
[22] Department of Physics & Astronomy, Clemson University, Kinard Lab of Physics, Clemson, SC 29634, USA
[23] Department of Aerospace, Physics and Space Sciences, Florida Institute of Technology, Melbourne, FL 32901, USA
[24] International Space Science Institute, Hallerstrasse 6, 3012 Bern, Switzerland
[25] Faculty of Law, Ryukoku University, Kyoto 612-8577, Japan
[26] Dipartimento di Fisica, Universitá di Trieste, I-34127 Trieste, Italy
[27] Istituto Nazionale di Fisica Nucleare, Sezione di Trieste, I-34127 Trieste, Italy
[28] INAF—Istituto di Radioastronomia, I-40129 Bologna, Italy
[29] Science and Technology Institute, Universities Space and Research Association, 320 Sparkman Drive, Huntsville, AL 35805, USA
[30] Kavli Institute for Astronomy and Astrophysics, Peking University, Beijing 100871, People's Republic of China
[31] National Astronomical Observatories, Chinese Academy of Sciences, Beijing 100012, People's Republic of China
[32] Department of Physics, University of Rome Tor Vergata, 00100 Rome, Italy
[33] Istituto Nazionale di Astrofisica, 00100 Rome, Italy
[34] Department of Space Science, University of Alabama in Huntsville, Huntsville, AL 35899, USA
Received 2024 May 17; revised 2024 June 24; accepted 2024 June 29; published 2024 July 19

Abstract

GW230529 is the first compact binary coalescence detected by the LIGO–Virgo–KAGRA collaboration with at least one component mass confidently in the lower mass gap, corresponding to the range 3–5 $M_{\odot}$. If interpreted as a neutron star–black hole merger, this event has the most symmetric mass ratio detected so far and therefore has a relatively high probability of producing electromagnetic (EM) emission. However, no EM counterpart has been reported. At the merger time t_0, Swift-BAT and Fermi-GBM together covered 100% of the sky. Performing a targeted search in a time window $[t_0 - 20\,\mathrm{s}, t_0 + 20\,\mathrm{s}]$, we report no detection by the Swift-BAT and Fermi-GBM instruments. Combining the position-dependent γ-ray flux upper limits and the gravitational-wave posterior distribution of luminosity distance, sky localization, and inclination angle of the binary, we derive constraints on the characteristic luminosity and structure of the jet possibly launched during the merger. Assuming a *top-hat* jet structure, we exclude at 90% credibility the presence of a jet that has at the same time an on-axis isotropic luminosity $\gtrsim 10^{48}$ erg s^{-1} in the bolometric band 1 keV–10 MeV and a jet opening angle $\gtrsim 15°$. Similar constraints are derived by testing other assumptions about the jet structure profile. Excluding GRB 170817A, the luminosity

Original content from this work may be used under the terms of the Creative Commons Attribution 4.0 licence. Any further distribution of this work must maintain attribution to the author(s) and the title of the work, journal citation and DOI.

upper limits derived here are below the luminosity of any GRB observed so far.

Unified Astronomy Thesaurus concepts: High energy astrophysics (739); Gamma-ray astronomy (628); Gamma-ray bursts (629); Gravitational waves (678)

1. Introduction

Since operations began in 2015, the LIGO–Virgo–KAGRA (LVK) detector network (Acernese et al. 2015; LIGO Scientific Collaboration et al. 2015; Akutsu et al. 2021) has successfully identified gravitational waves (GWs) consistent with binary black hole (BBH) mergers, binary neutron star (BNS) mergers, and neutron star–black hole (NSBH) mergers (Abbott et al. 2021a, 2023). NSBH mergers, like BNS mergers, can be accompanied by a short γ-ray burst (GRB) and/or a kilonova emission, with the kilonova due to the radioactive decay of heavy elements in the neutron-rich ejecta launched by the merger (Rosswog 2005; Tanaka et al. 2014; Ciolfi 2018; Metzger 2019; Gompertz et al. 2020, 2023; Zhu et al. 2022). The intrinsic brightness of the electromagnetic (EM) emission strongly depends on the amount of mass released before the NS enters the innermost stable circular orbit of the BH, impacted in turn by the mass ratio and the magnitude and orientation of the spins of the two objects (Kawaguchi et al. 2015; Foucart et al. 2018; Krüger & Foucart 2020). Specifically, low-mass BHs, more compact NSs, and high prograde spins are all factors that favor tidal disruption and make the NSBH candidate potentially EM-bright. Moreover, additional conditions are required for an NSBH merger to successfully launch a relativistic jet (Barbieri et al. 2020; Colombo et al. 2024). On average, NSBH mergers have a smaller probability of having enough material to be collimated in a jet, compared to BNS mergers, though they have the advantage that the polar axis is not expected to be baryon polluted, facilitating the propagation and acceleration of the relativistic outflow (Kyutoku et al. 2015).

Among all the compact binary merger candidates found by the LVK collaboration up to the time of writing, GW191219_163120 and GW200115_042309 are confidently classified as NSBH mergers with $p_{\rm astro} > 0.5$ (Abbott et al. 2021b, 2023; Fletcher et al. 2024).[35] Focusing on GW200115_042309, this merger was found to have a 27%–30% probability that the primary component falls within the range of the lower mass gap depending on the choice of spin prior (Abbott et al. 2021b). Further analysis indicated that $<10^{-6}\ M_{\odot}$ was ejected from this merger at >99% credibility, based on calculations of dynamical ejecta and mass loss due to disruption (Abbott et al. 2021b). This is consistent with the nondetection of EM emission accompanying these candidates (Anand et al. 2021; Dichiara et al. 2021; Zhu et al. 2021; Fletcher et al. 2024).

In addition, GW190814 and GW200210_092254 are particularly noteworthy, since the inferred secondary mass of $2.59^{+0.08}_{-0.09}\ M_{\odot}$ (for GW190814) and $2.6^{+0.1}_{-0.1}\ M_{\odot}$ (for GW200210_092254) indicates that the source could have been an extremely massive NS or a BH (Abbott et al. 2020, 2021a, 2023). Neither of these NSBH candidates were found to have associated EM emission in their follow-up observations (Dobie et al. 2019; Thakur et al. 2020; Watson et al. 2020; Alexander et al. 2021; Kilpatrick et al. 2021; Fletcher et al. 2024).

[35] At the time, GW200105_162426 was also identified as an NSBH candidate. Subsequent analysis found this trigger to be of marginal interest with $p_{\rm astro} < 0.5$ (Abbott et al. 2023).

Given the lack of a direct association, there is still no consensus about the fraction of short GRBs potentially driven by NSBH mergers. However, Biscoveanu et al. (2023) find an upper limit of $20\ {\rm Gpc}^{-3}\ {\rm yr}^{-1}$ on the rate of GRBs with NSBH progenitors based on the population of mergers observed in GWs. Whether there exists a subpopulation of short GRBs whose distinctive properties could distinguish these merger channels remains unsettled. Several studies have tried to explore such a dichotomy deeper by examining samples of short GRBs through some of their observable properties, such as duration, energetics, kilonova emission, locations, and offsets from host galaxies (Troja et al. 2008; Gompertz et al. 2020; Dimple & Arun 2023). These studies suggest that short GRBs with extended emission could indeed be classified as a unique population that potentially arises from NSBH mergers. Moreover, depending on the amount of disk mass and the accretion timescale, NSBH mergers can power GRBs whose duration extends well beyond the canonical 2 s, as observed for the two merger-driven long-duration bursts: GRB 211211A (Mei et al. 2022; Rastinejad et al. 2022; Troja et al. 2022; Yang et al. 2022) and GRB 230307A (Levan et al. 2024; Yang et al. 2024).

The paucity of significant detections of NSBH mergers in previous LVK observing runs limits our understanding of the NSBH population, the associated merger rate, and the probability of producing a bright EM emission. Detecting these events through their γ-ray emission or setting sensitive upper limits will allow us to derive constraints on the parameters associated with the various predicted GRB jet emission models and subsequently allow us to potentially differentiate better the BNS and NSBH merger channels (Burns 2020). Moreover, since the quality of GW data is not always good enough to confirm or exclude with confidence the presence of an NS in a compact binary merger, the detection of an EM counterpart would be the smoking gun to prove the presence of baryonic matter surrounding the final remnant object. Past multimessenger studies have already demonstrated how the combination of GW data and γ-ray observations could shed light on the association between BNS/NSBH mergers and short GRBs, as well as on the jet properties, including the opening angle and structure profile (Biscoveanu et al. 2020; Farah et al. 2020; Hayes et al. 2020, 2023).

In this work, we examine the nondetection of γ-ray emission from the GW trigger GW230529_181500, hereafter GW230529 (Abac et al. 2024a), based on the monitoring from Swift-BAT and Fermi-GBM. We summarize the GW properties of this NSBH event in Section 2. In Sections 3 and 4 , we discuss the Swift-BAT and Fermi-GBM observations and the targeted search analysis that was conducted around the trigger time of the event. Using joint BAT–GBM flux upper limits (Section 5), we further discuss the methods adopted to place constraints on the jet luminosity and opening angle (Section 6). We discuss the simulations in Section 7 and present our results in Section 8.

2. Information from the GW Analysis

Abac et al. (2024a) report that GW230529 is a compact binary coalescence whose primary is an NS of mass $1.4^{+0.6}_{-0.2}\ M_{\odot}$

merging with a compact object of mass $3.6^{+0.8}_{-1.2}$ $M_\odot$ at 90% credibility. In the hypothesis of a highly spinning secondary component and marginalizing over the component mass distributions and the NS equation of state (EoS), there is a <10% probability that the NS is tidally disrupted. The corresponding ejected mass due to the tidal disruption of the NS is <0.052 $M_\odot$ at 99% credibility. This limit is quite informative, since, under optimal conditions, NSBH mergers can eject up to ∼0.1–0.3 $M_\odot$ (e.g., Kyutoku et al. 2015). With the detection of GW230529, we now know that events with low mass ratios exist, increasing the probability that the NSBH class of events can be EM-bright. Indeed, with the inclusion of GW230529 in the sample of NSBHs detected so far, Abac et al. (2024a) derive that up to 18% of the population can power an EM counterpart, a factor of 3 larger compared to the same analysis that excluded GW230529. The authors also report that, due to the higher probability of having a tidal disruption of the NS, the upper bound on the rate of GRBs coming from NSBH progenitors increases to a value of 23 $\mathrm{Gpc^{-3}\ yr^{-1}}$, based on the methodology developed by Biscoveanu et al. (2023).

The uncertainty in the sky localization is remarkably large, covering almost the totality of the sky (≃24,100 $\mathrm{deg^2}$ at 90% credibility). The luminosity distance is constrained in the range $D_L = 201^{+102}_{-96}$ Mpc ($z \sim 0.045$). The posterior distribution of the inclination angle of the binary is uninformative, being very close to the detection prior, which follows the Malmquist bias (see, e.g., Schutz 2011). The posterior samples required for this analysis are downloaded from the LVK data release repository (Abac et al. 2024b). Here we consider the posterior samples labeled as `Combined _PHM _highSpin`, which are the combination of posteriors obtained independently using the `IMRPhenomXPHM` (Pratten et al. 2021) and `SEOBNRv4PHM` (Ossokine et al. 2020) waveforms, in the assumption of a high-spin prior for both components. For consistency, throughout the Letter, we use the corresponding sky localization map `skymap _combined _PHM _high _spin.fits`.

An independent follow-up analysis performed by Zhu et al. (2024) finds that, considering APR4 (Akmal et al. 1998) and DD2 (Typel et al. 2010) as EoSs, the probability that in the merger the NS is tidally disrupted is 12.8% and 63.2%, respectively. Moreover, combining this event with population models of NSBH mergers, the authors find that >90% of tidally disrupted NSBHs come from the subclass of events where the primary mass is in the [3–5] $M_\odot$ mass range. From the detectability perspective, due to the small mass ratio between the BH and NS, the higher chance of having matter around the central remnant implies that the rate of detectable GRBs (within 300 Mpc) formed by NS+[3–5] $M_\odot$ systems is at least a factor of 10 larger than the rate of GRBs formed by NS+[>5] $M_\odot$ systems. The factor is even larger for the detectability of the kilonova component.

Numerical simulation performed by Martineau et al. (2024) in the mass regime of GW230529 reveals the possible emergence of a low-mass accretion disk capable of powering a short GRB (Gottlieb et al. 2023). Therefore, it is evident that events like GW230529 are, among NSBH mergers, the most promising candidates to have an associated EM emission, in the form of a GRB and/or kilonova emission. Any constraint on the EM nature of these systems is notably valuable to obtain deeper insights about the connection between the merger parameters (component masses, spins, and inclination angle) and the capability to power GRB/kilonova emission.

3. Swift-BAT Observation

The Neil Gehrels Swift Observatory (Gehrels et al. 2004), launched in 2004, has successfully detected and localized >1600 GRBs in its almost 20 yr of operations. This is thanks in most part to its GRB monitor, Swift-BAT (Barthelmy et al. 2005). Swift-BAT is a wide field-of-view (∼2 sr), coded mask imager that is sensitive to γ-rays in the 15–350 keV energy range. By correlating the spatial distribution of detected counts across Swift-BAT's detector plane with the pattern of its coded mask, an image of the sky can be created, and sources can be localized within a few arcminutes.

At the trigger time of GW230529, Swift was in a pointed observation and a good data-taking mode. There were no onboard GRB triggers within 1 hr of GW230529.

During the full period of O4, the Gamma-ray Urgent Archiver for Novel Opportunities (GUANO; Tohuvavohu et al. 2020) enables the downlink of Swift-BAT data for all the GW triggers with a false-alarm rate of $<2\,\mathrm{day^{-1}}$. For GW230529, GUANO downloaded 200 s of event data around the trigger time. We performed a targeted search with the NITRATES pipeline (DeLaunay & Tohuvavohu 2022) in a temporal window $[t_0 - 20\,\mathrm{s},\ t_0 + 20\,\mathrm{s}]$, where $t_0 =$ 2023-05-29T18:15:00 UTC is the GW trigger time. The analysis searched for impulsive γ-ray emission over eight different timescales: 0.128, 0.256, 0.512, 1.024, 2.048, 4.096, 8.192, and 16.384 s. The most significant candidate identified by the search has a $\sqrt{\mathrm{TS}} = 5.7$, which corresponds to a false-alarm rate $>0.01\,\mathrm{s^{-1}}$. $\sqrt{\mathrm{TS}}$ is defined in DeLaunay & Tohuvavohu (2022) and gives the statistical significance of the detection. With these search results, we find no significant evidence of a possible γ-ray signal associated with GW230529. With a nondetection, upper limits are set with the method introduced in Fletcher et al. (2024) but with added responses for positions outside the coded field of view to make the upper limits cover the full Earth unocculted sky.

We derive flux upper limits considering a temporal bin of 1 s with a confidence level of 5σ, unless otherwise stated. The choice of the temporal bin is made according to the theoretical expectation of the typical duration of GRBs originated by NSBH systems. We consider three spectral templates, consisting of a Band function (Band et al. 1993), with a peak energy of 75 keV (soft template), 230 keV (normal template), and 1500 keV (hard template), while the low- and high-energy photon indices are fixed to $\alpha = -1$ and $\beta = -2.3$, respectively. As discussed in Section 6, we have no strong priors on the inclination angle of the binary; therefore, it would be unmotivated to assume a peak energy typical of on-axis short-hard GRBs. Therefore, for each pixel of the sky map, we consider the spectral template that produces the largest value of the flux upper limit. In this way, the adopted upper limit is the most conservative one, without impacting the solidity of our conclusions.

If P_{GW} is the GW sky localization probability, ϵ_{cov} is the probability that the GW event occurred in a position of the sky not occulted by the Earth, and $\epsilon_{\mathrm{in\ FoV}}$ is the probability that the GW event occurred inside the BAT coded field of view, we have

$$\epsilon_{\mathrm{cov}} = 1 - \int_{\Omega \in \Omega_\oplus} P_{\mathrm{GW}}(\Omega) d\Omega \quad (1)$$

and

$$\epsilon_{\mathrm{in\ FoV}} = \int_{\Omega \in \Omega_{\mathrm{BAT}}} P_{\mathrm{GW}}(\Omega) d\Omega, \quad (2)$$

where Ω denotes the sky coordinates. We obtain the values $\epsilon_{\rm cov} = 63\%$ and $\epsilon_{\rm in\ FoV} = 15\%$.

4. Fermi-GBM Observation

Fermi-GBM consists of 12 sodium iodide (Na I) and two bismuth germanate (BGO) detectors that cover the full sky, unocculted by the Earth (Meegan et al. 2009). The Na I detectors are sensitive to photons in the energy range 8 keV–1000 keV, and the BGO detectors observe the 200 keV–40 MeV energy range. The flight software on board Fermi-GBM triggers on any event with a flux of γ-rays at a level greater than a threshold (typically $\sim 4.5\sigma$–5σ) above the background rate in at least two Na I detectors (von Kienlin et al. 2020). In more than 15 yr of operations, Fermi-GBM has detected more than 3750 GRBs with onboard triggers.

In addition to trigger data, Fermi-GBM gives us high time resolution (2 μs) data in the form of continuous time tagged events (CTTEs) over the energy range from 8 keV to 40 MeV. The CTTE data allow us to search for GRBs below Fermi-GBM's onboard trigger threshold using ground-based computing resources (Blackburn et al. 2015; Goldstein et al. 2019). The most sensitive search method, referred to as the *Targeted Search* pipeline, is a likelihood-based approach for multi-messenger follow-up observations (Blackburn et al. 2015). More details about the *Targeted Search* pipeline can be found in Blackburn et al. (2015), Goldstein et al. (2019), Hamburg et al. (2020), and Fletcher et al. (2024).

At the merger time of GW230529, a fraction $\epsilon_{\rm cov} = 62\%$ of the GW localization was visible to Fermi-GBM. There was no onboard trigger near this time. We therefore performed a search for GRB-like emission with *Targeted Search* from ± 20 s around the merger time. The scan was repeated for nine characteristic emission timescales that increased by factors of 2 from 64 ms to 16.384 s using the three characteristic GRB spectra from Table 3 of Fletcher et al. (2024). No significant counterparts were identified by this search.

As we did not find a significant counterpart in Fermi-GBM for GW230529, we compute the γ-ray flux upper limits as a function of sky position using the pipeline *Targeted Search*. We do this by computing the upper limits, with a 5σ confidence level, separately for each spectral template. Similar to Swift-BAT, we then choose the least constraining limit from all three spectral templates for each position to obtain a final upper limit, which is less sensitive to the individual spectral shapes.

5. Joint BAT+GBM Flux and Luminosity Upper Limits

We combine the flux upper limits from Swift-BAT and Fermi-GBM, indicated as $\mathrm{UL}_{\rm BAT}(\Omega)$ and $\mathrm{UL}_{\rm GBM}(\Omega)$, respectively, producing a joint flux upper limit map defined as

$$\mathrm{UL}_{\rm joint}(\Omega) = \min[\mathrm{UL}_{\rm BAT}(\Omega), \mathrm{UL}_{\rm GBM}(\Omega)]. \quad (3)$$

The map is shown in the upper left panel of Figure 1, superimposed on the contour levels of the GW sky localization. The flux upper limits are reported in the 15–350 keV energy band. Lighter colored regions indicate more sensitive upper limits. The solid and dashed lines are the GW sky localization contours at 90% and 50% credibility, respectively. The single Swift-BAT and Fermi-GBM flux upper limits maps are shown in the Appendix (Figure 11), where the white region indicates the fraction of the sky covered by the Earth.

We also compute a sky-dependent bolometric luminosity upper limit in the rest-frame energy band 1 keV–10 MeV as

$$L_{\rm UL}(\Omega) = 4\pi \bar{D}_L^2(\Omega) k(\Omega) \mathrm{UL}_{\rm joint}(\Omega), \quad (4)$$

where

1. $\bar{D}_L(\Omega)$ is the mean luminosity distance as a function of the sky position. This in turn is derived as

$$\bar{D}_L(\Omega) = \int D_L P_{D_L}(D_L|\Omega) dD_L, \quad (5)$$

with $P_{D_L}(D_L|\Omega)$ the sky-position-dependent posterior distribution of the luminosity distance.

2. $k(\Omega)$ is the k-correction, defined as

$$k(\Omega) = \frac{I[1\ \mathrm{keV}/(1+z(\Omega)),\ 10\ \mathrm{MeV}/(1+z(\Omega))]}{I[15\ \mathrm{keV},\ 350\ \mathrm{keV}]}, \quad (6)$$

where

$$I[a, b] = \int_a^b E \frac{dN}{dE}(\Omega) dE, \quad (7)$$

and $dN/dE(\Omega)$ is the assumed photon spectrum. For the computation of $z(\Omega)$, we adopt the values of Planck Collaboration et al. (2020), namely, $h = 0.68$, $\Omega_\Lambda = 0.69$, and $\Omega_m = 0.31$.

The sky map of $L_{\rm UL}(\Omega)$ is shown in the upper right panel of Figure 1. In the lower panel of Figure 1, we show the distribution of $L_{\rm UL}(\Omega)$ over all the sky pixels. The distribution $N_W(L_{\rm UL})$ is obtained considering the collection $L_{\rm UL}(\Omega_i)$ for each pixel i and weighted by the GW sky probability density $P_{\rm GW}(\Omega_i)$. $N_W(L_{\rm UL})$ shows a double peak, the lower one being due to the more constraining upper limits obtained by Fermi-GBM and Swift-BAT (inside the field of view), while the higher one is due to the less constraining values obtained outside the Swift-BAT field of view. The vertical dashed line in the lower panel of Figure 1 reports the weighted average of $L_{\rm UL}(\Omega)$, defined as

$$\langle L_{\rm UL} \rangle = \int L_{\rm UL}(\Omega) P_{\rm GW}(\Omega) d\Omega = 2.5 \times 10^{48} \mathrm{erg\ s^{-1}}. \quad (8)$$

6. Constraining the γ-Ray Emission from GW230529

The nondetection of any γ-ray signal coincident with GW230529 can be interpreted as follows. In the NSBH merger scenario, one possibility is that the NS is entirely swallowed by the BH and the absence of any accretion material prevents the formation and launch of a relativistic jet, necessary for the GRB emission. On the other hand, even if a jet is launched, it might be too off-axis to produce any detectable γ-ray signal. A third option is that the amount of material accreted onto the central engine is so scarce that the resulting jet, even if aligned with the observer, is not powerful enough to produce a detectable γ-ray signal. Additionally, since there are no constraints on the tidal deformability of the secondary component, it is not excluded that GW230529 is an exotic merger of unusually light BHs, possibly of primordial origin (e.g., Escrivà et al. 2022; Huang et al. 2024). In this last case, unless the BBH merger is embedded in a very dense environment (Graham et al. 2023), no EM counterpart is expected.

The aim of this section is to exploit the nondetection upper limits of Swift-BAT and Fermi-GBM to infer possible

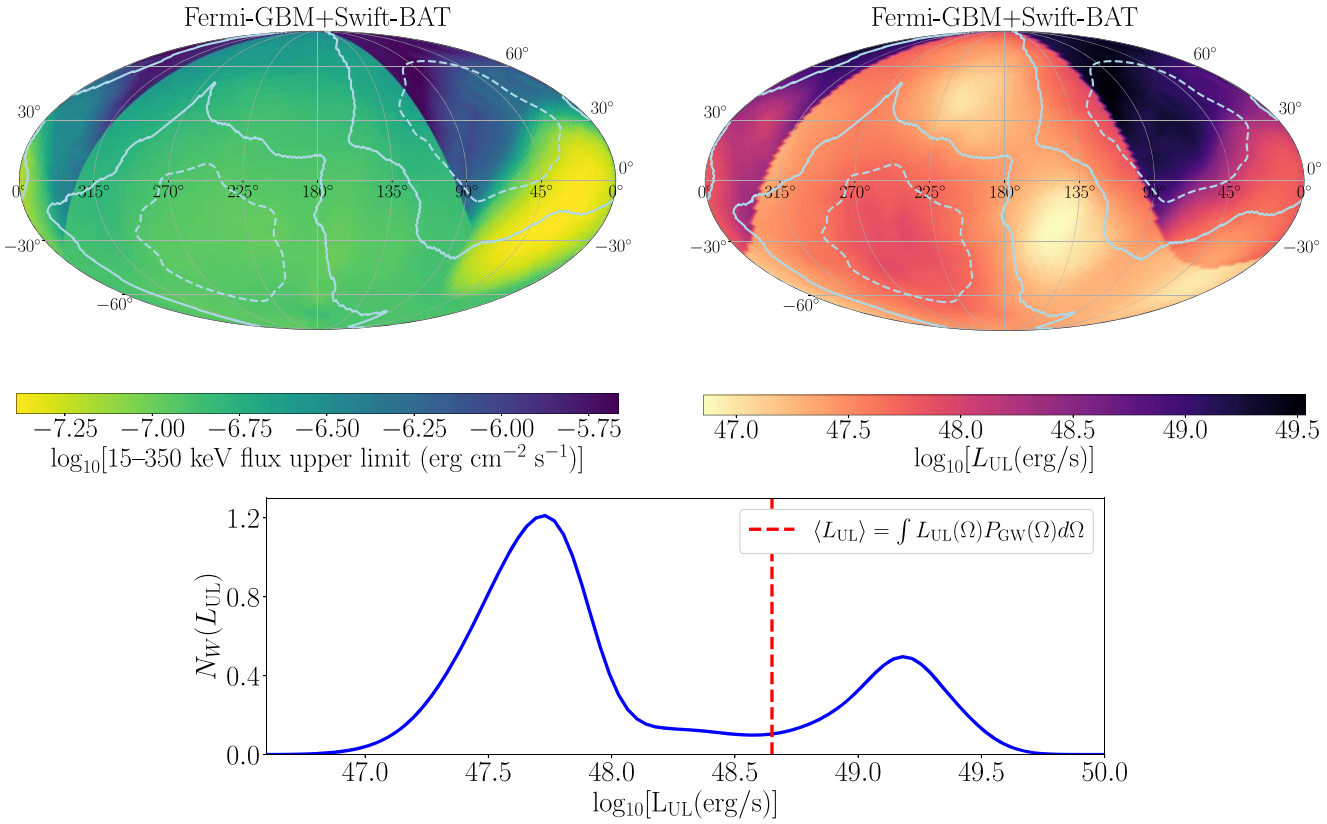

Figure 1. Upper left panel: joint Swift-BAT+Fermi-GBM flux upper limit sky map in the 15–350 keV band. The upper limits are relative to a timescale of 1 s, computed at 5σ confidence level. For the individual contributions from the two telescopes, see Figure 11. Upper right panel: joint Swift-BAT+Fermi-GBM sky map of the bolometric luminosity upper limit. The luminosity is computed in the rest-frame energy range 1 keV–10 MeV. In both upper panels, the solid and dashed lines are the GW localization contours at 90% and 50% credibility, respectively. Lower panel: weighted distribution of the luminosity upper limit, where the weight is given by the GW probability density of the single pixel. The vertical dashed line represents the weighted average over the sky of the luminosity upper limit.

constraints on the typical luminosity of the jet. As expected from theoretical simulations and confirmed by observations, the jets of GRBs have an angular structure that can deviate from the top-hat approximation (Rossi et al. 2002; Granot & Kumar 2003; Abbott et al. 2017; Lamb & Kobayashi 2017; Troja et al. 2017, 2018, 2019; Ghirlanda et al. 2019; Ryan et al. 2020; Salafia & Ghirlanda 2022). In general, the jet structure can be described by a core with opening angle θ_c, where the energy radiated per unit solid angle $E(\theta_v)$ is approximately constant, and an off-core region, where the radiated energy drops off rapidly as a function of the inclination angle. Here we construct a simple toy model to describe the analytical form of the apparent structure of the jet luminosity, namely, as measured by an observer located at an inclination angle θ_v from the jet axis. Formally, the apparent structure of luminosity $L(\theta_v)$ does not necessarily follow the same profile of $E(\theta_v)$ (see the Appendix for further details). We parameterize the apparent structure of the jet luminosity as

$$L(\theta_v) = L_0 l(\theta_v), \tag{9}$$

where $L_0 = L(\theta = 0)$, while

$$l(\theta_v) = \begin{cases} \sim 1, & \theta < \theta_c \\ f(\theta_v), & \theta > \theta_c \end{cases}. \tag{10}$$

In the following, we focus on five possible profiles of the jet structure.

1. *Top-hat*:

$$l(\theta_v) = \begin{cases} 1, & \theta < \theta_c \\ 0, & \theta > \theta_c \end{cases}. \tag{11}$$

2. *Gaussian*:

$$l(\theta_v) = \exp\left[-\frac{\theta_v^2}{2\theta_c^2}\right]. \tag{12}$$

3. *Power law*:

$$l(\theta_v) = \frac{1}{1 + \left(\frac{\theta_v}{\theta_c}\right)^s}. \tag{13}$$

4. *Two components*:

$$l(\theta_v) = \begin{cases} 1, & \theta < \theta_c \\ L_{\rm off}/L_0, & \theta > \theta_c \end{cases}. \tag{14}$$

This structure consists of a *top-hat* plus an isotropic component outside the jet core.

5. *Isotropic*:

$$l(\theta_v) = 1. \tag{15}$$

For completeness, we also explore the possibility that this GW merger did not produce a jetted GRB-like emission but rather a more isotropic component whose nature could be associated with the precursor emission and/or the extended emission typically observed in merger-

driven GRBs. Since this kind of emission can occur on longer timescales (∼tens of seconds), we consider an upper limit computed on the timescale of 16.384 s, the longest available from the templates.

The apparent luminosity $L(\theta_v)$ has to be interpreted as the rest-frame luminosity computed in the bolometric energy range 1 keV–10 MeV. Moreover, the luminosity defined here does not need the definition of a spectral model. As explained more in detail in the Appendix, given a limit on $L(\theta)$, one can derive a constraint on the spectrum normalization once the spectral shape is known. This is in line with the derivation of a flux upper limit using a set of different spectral templates.

7. Simulation Setup

The aim of this section is to set up a simulation that combines the posterior distribution of the GW parameters with the sky-position-dependent upper limits of Swift-BAT $\mathrm{UL_{BAT}}(\Omega)$ and Fermi-GBM $\mathrm{UL_{GBM}}(\Omega)$ in order to infer constraints about the parameters of the jet structure. As specified in Section 5, for each pixel of the sky, we consider an upper limit

$$\mathrm{UL}(\Omega) = \mathrm{UL_{joint}}(\Omega), \tag{16}$$

defined by Equation (3). To derive constraints on the luminosity in the bolometric range 1 keV–10 MeV, we apply for each pixel of the sky map a bolometric correction to $\mathrm{UL}(\Omega)$ considering the spectral template that produces the largest, and hence most conservative, flux upper limit in the same energy band. From the posterior samples of GW230529, we extract the distribution of sky position, luminosity distance, and inclination angle. Among these parameters, only the inclination angle is a free parameter in our modeling, while we do not make any further inference about the sky position and the distance. Calling $\boldsymbol{\theta}$ the set of intrinsic parameters of the jet structure, the likelihood of the model is defined as

$$\mathcal{L}(\boldsymbol{\theta}, \theta_v) = P_{ND}(\boldsymbol{\theta}, \theta_v), \tag{17}$$

corresponding to the probability of nondetection.

For a fixed combination of $(\boldsymbol{\theta}, \theta_v)$, the nondetection probability also depends on the distance and the sky coordinates, since the sensitivity of the γ-ray monitors changes as a function of the sky position. The nondetection probability can be explicated as

$$P_{\mathrm{ND}}(\boldsymbol{\theta}, \theta_v) = \times \int P(F < \mathrm{UL}(\Omega)) P_{\mathrm{GW}}(\Omega, D_L|\theta_v) d\Omega dD_L, \tag{18}$$

where $P(F < \mathrm{UL}(\Omega))$ is the probability that, having fixed the parameters $(\boldsymbol{\theta}, \Omega, D_L, \theta_v)$, the observed flux is below the upper limit $\mathrm{UL}(\Omega)$, while Ω is the sky position (R.A., decl.), D_L is the luminosity distance, and $P_{\mathrm{GW}}(\Omega, D_L|\theta_v)$ is the corresponding conditional probability distributions extracted from the GW posteriors, which in turn depend on θ_v. The function $\mathcal{L}(\boldsymbol{\theta}, \theta_v)$ has been evaluated by injecting sources according to the distributions $P_{\mathrm{GW}}(\Omega, D_L|\theta_v)$. The nondetection probability is computed by counting the fraction of injected sources that produced an observed flux in the 1 keV–10 MeV band lower than the upper limit $\mathrm{UL}(\Omega)$.

According to the Bayes theorem, we computed the posterior distribution as

$$\mathcal{P}(\boldsymbol{\theta}, \theta_v) \propto \mathcal{L}(\boldsymbol{\theta}, \theta_v) \prod_j \pi(\theta_j), \tag{19}$$

where $\pi(\theta_j)$ are the respective priors. As mentioned before, $\pi(\theta_v)$ corresponds to the GW posterior of the viewing angle. For the model parameters L_0, L_{off}, θ_c, and s, we consider uniform priors

$$\pi[\log(L_0)] = \begin{cases} \text{const}, & 45 < \log[L_0(\mathrm{erg\ s^{-1}})] < 55 \\ 0, & \text{otherwise} \end{cases}, \tag{20}$$

$$\pi[\log(L_{\mathrm{off}})] = \begin{cases} \text{const}, & 40 < \log[L_{\mathrm{off}}(\mathrm{erg\ s^{-1}})] < 50 \\ 0, & \text{otherwise} \end{cases}, \tag{21}$$

$$\pi(\theta_c) = \begin{cases} \text{const}, & 0.^\circ 1 < \theta_c < 30^\circ \\ 0, & \text{otherwise} \end{cases}, \tag{22}$$

$$\pi(s) = \begin{cases} \text{const}, & 1 < s < 10 \\ 0, & \text{otherwise} \end{cases}. \tag{23}$$

The choice of $\pi[\log(L_0)]$ fully covers the range of possible luminosities a GRB could have, from the subluminous regime to the typical values of cosmological GRBs (e.g., Fong et al. 2015). The boundaries in the prior $\pi(\theta_c)$ are compatible with previous values of half-jet opening angles derived in the literature (Fong et al. 2015; Troja et al. 2016; Lamb et al. 2019; Rouco Escorial et al. 2023). The prior of L_{off}, instead, is bounded to lower values, since the off-axis emission of a GRB is expected to be less Doppler boosted and, therefore, subluminous with respect to the on-axis component (Ramirez-Ruiz et al. 2002; Lazzati et al. 2017a, 2017b; Nakar & Piran 2017; Gottlieb et al. 2018; Hamidani & Ioka 2023). The distribution $\pi(\theta_v)$, corresponding to the GW posterior $P_{\mathrm{GW}}(\theta_v)$, is close to being symmetric around $\pi/2$. Moreover, the jet emission is assumed to be symmetric with respect to the binary orbital plane, namely, $L(\theta_v) = L(\pi - \theta_v)$; therefore, we hereafter consider the inclination angle θ_v only in the range $[0, \pi/2]$. This is obtained by creating a prior

$$\pi(\theta_v) = \begin{cases} P_{\mathrm{GW}}(\theta_v) + P_{\mathrm{GW}}(\pi - \theta_v), & 0 < \theta_v < \dfrac{\pi}{2} \\ 0, & \text{otherwise} \end{cases}, \tag{24}$$

and then renormalized to have $\int \pi(\theta_v) d\theta_v = 1$. For the derivation of the posterior distribution, we adopt the following approaches.

1. We perform a numerical evaluation of the likelihood for all the models with three or fewer free parameters, namely, the *top-hat*, the *Gaussian*, the *power law* with fixed s, and the *isotropic* models. Each model parameter is sampled in a linearly spaced bin of 30 elements.
2. The `emcee` sampler (Foreman-Mackey et al. 2013) is used for all the models with more than three free parameters, namely, the *power-law* with free s and the *top-hat+isotropic* component. The convergence of the chain is controlled by imposing that the autocorrelation time is larger than 50 times the number of steps.

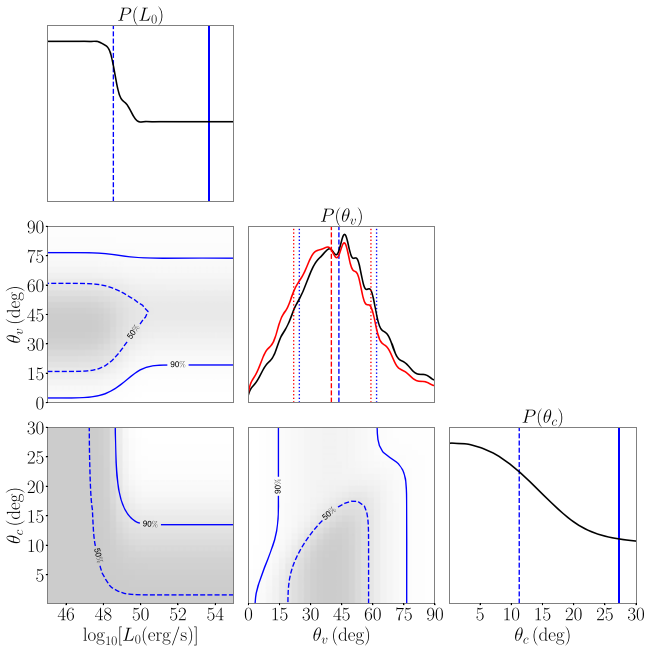

Figure 2. Corner plot of the posterior distribution for the parameters L_0, θ_c, and θ_v, assuming a *top-hat* jet structure. In the off-diagonal plots, the dashed and solid lines indicate the 50% and 90% credible regions. In the middle panel $P(\theta_v)$, we report in red the prior $\pi(\theta_v)$ derived from the GW analysis. The vertical dotted lines identify the 1σ credible interval (16th and 84th percentiles), while the dashed lines are the median (50th percentile). For the other posteriors, $P(L_0)$ and $P(\theta_c)$, the vertical dashed and solid lines report the 50th and 90th percentiles of each posterior, respectively. The gray scale in the off-diagonal plots indicates the posterior density, where darker corresponds to larger values. The excluded regions are outside the gray areas.

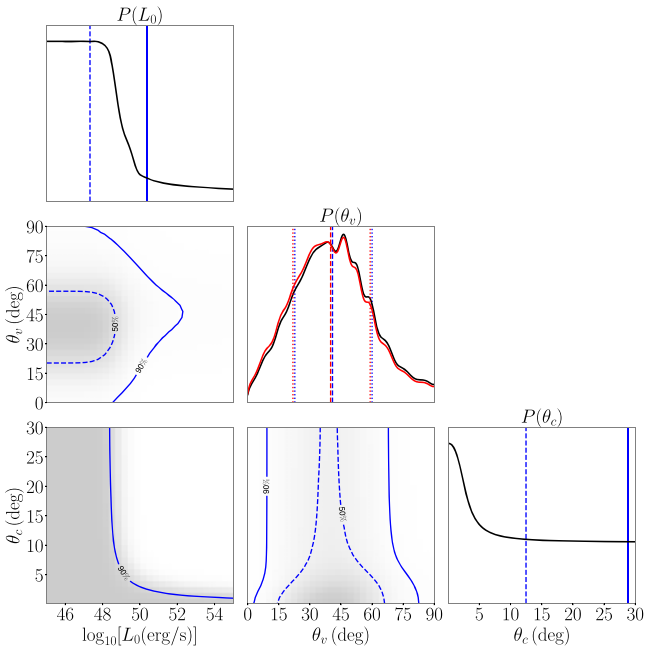

Figure 3. Same as Figure 2 but assuming a *Gaussian* profile for the jet structure.

8. Results and Discussion

The corner plot of the posterior distribution of L_0, θ_c, and θ_v is shown in Figure 2 for the *top-hat* structure, Figure 3 for the *Gaussian*, and Figure 4 for the *power law* with $s = 2$ and $s = 4$, respectively. Darker regions inside each panel indicate where the posterior probability is higher. Therefore, the excluded regions are outside the gray areas. Focusing on the *top-hat* plot, we note the following.

1. Analyzing the θ_c–L_0 posterior panel, we can derive that a jet configuration with $L_0 \gtrsim 10^{48}$ erg s^{-1} and $\theta_c \gtrsim 15°$ is excluded at 90% credibility.
2. Analyzing the $\theta_v - L_0$ posterior panel, we can conclude that, if the jet had an on-axis luminosity of $L_0 \gtrsim 10^{50}$ erg s^{-1}, our analysis implies that the viewing angle could not be smaller than $\sim 15°$ at 90% credibility, independent of the opening angle of the jet and the assumption about the jet structure.
3. From the comparison in the central panel between the prior $\pi(\theta_v)$ and the posterior $P(\theta_v)$, our analysis shows an overall marginal preference for larger values of θ_v.

Very similar behaviors are present in the corner plots of the other jet structures, with the major difference being that the 90% exclusion region in the θ_c–L_0 posterior panel extends to lower values of θ_c. Such a behavior is expected, since all the jet profiles that differ from a *top-hat* also have emission outside θ_c, implying more stringent constraints on this parameter.

Considering the posterior distribution of L_0, especially in the *top-hat* scenario, it is evident that $P(L_0)$ flattens and stays constant for values above $\sim 10^{50}$ erg s^{-1}. This can be explained as follows. Let us consider two values of L_0 and the corresponding likelihoods $P(L_{0,a})$ and $P(L_{0,b})$. If both $L_{0,a}$ and $L_{0,b}$ are large enough, then whenever $\theta_v < \theta_c$, the predicted flux is above the derived upper limit. Namely,

$$P(F < \mathrm{UL}(\Omega)) \sim \Theta(\theta_v - \theta_c), \tag{25}$$

where $\Theta(x)$ is a step function. Therefore, the likelihood becomes independent of L_0 and saturates to a constant value equal to

$$\mathcal{L}(L_0, \theta_c, \theta_v) \tag{26}$$

$$= \int \Theta(\theta_v - \theta_c) P_{\mathrm{GW}}(\Omega, D_L|\theta_v) d\Omega dD_L. \tag{27}$$

In Figure 5, we show the corner plot for the *power-law* structure with free s (top panel) and the *top-hat+isotropic* component (bottom panel). For the *power-law* structure, as expected, the posterior distribution of s peaks at high values, giving preference to a jet whose off-axis emission sharply drops outside the core. From the θ_c–L_0 correlation plot, we can see that for a representative value of $\theta_c \sim 10°$ (typical of standard GRBs), our analysis imposes an upper limit on the on-axis isotropic luminosity of $\sim 10^{51}$ erg s^{-1} (90% credibility). For the *top-hat+isotropic* component structure, the L_0 and θ_c parameters are more poorly constrained with respect to the other structures. On the other hand, the off-axis luminosity L_{off} is constrained to be $\lesssim 10^{48}$ erg s^{-1} (90% credibility).

The plot in Figure 6 shows the posterior distribution of the apparent luminosity for a hypothetical subluminous isotropic emission. Since the flux upper limits for this model are computed using a temporal bin of 16.384 s, L_0 has to be the average luminosity on the same timescale. The 90% credible upper limit on L_0 is 8.5×10^{47} erg s^{-1}.

In Figure 7, we show the posterior probability map of the luminosity profile $L(\theta_v)$ for each jet structure. The map is obtained by extracting the jet structure parameters (L_0, θ_c, s, L_{off}) from the respective posterior distributions for each jet structure considered in this work. For a given fixed value of θ_v,

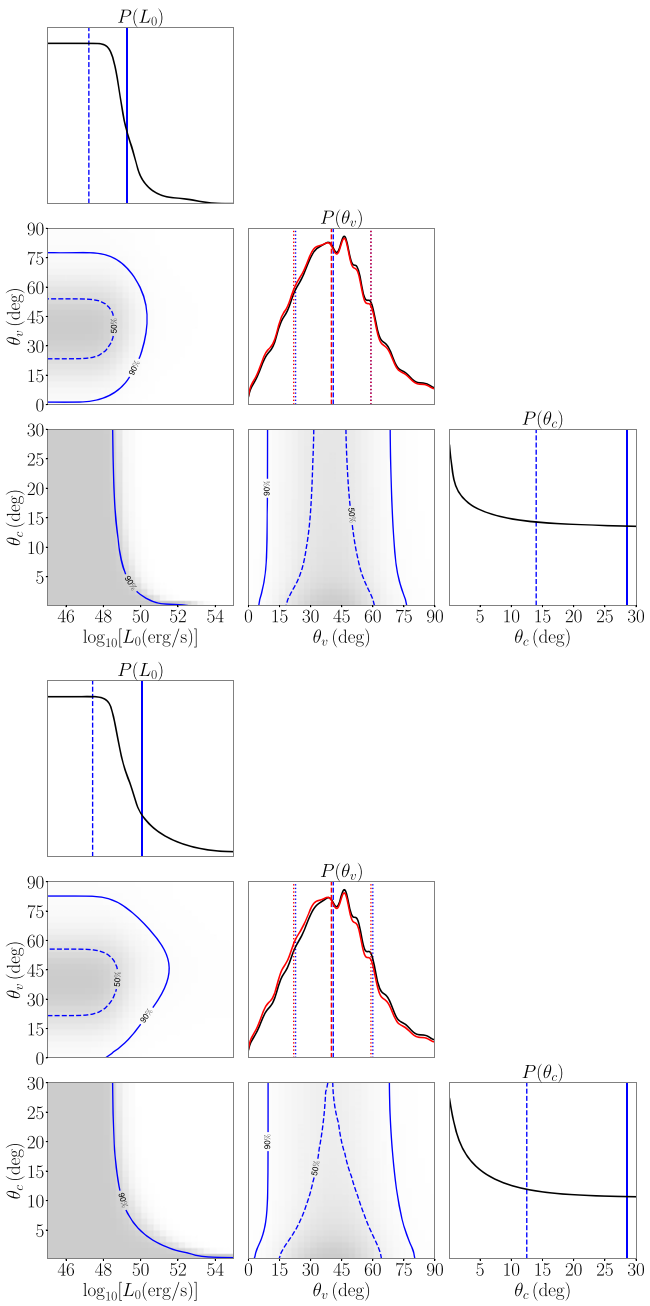

Figure 4. Same as Figure 2 but assuming a power-law profile for the jet structure with an off-axis slope $s = 2$ (top) and $s = 4$ (bottom).

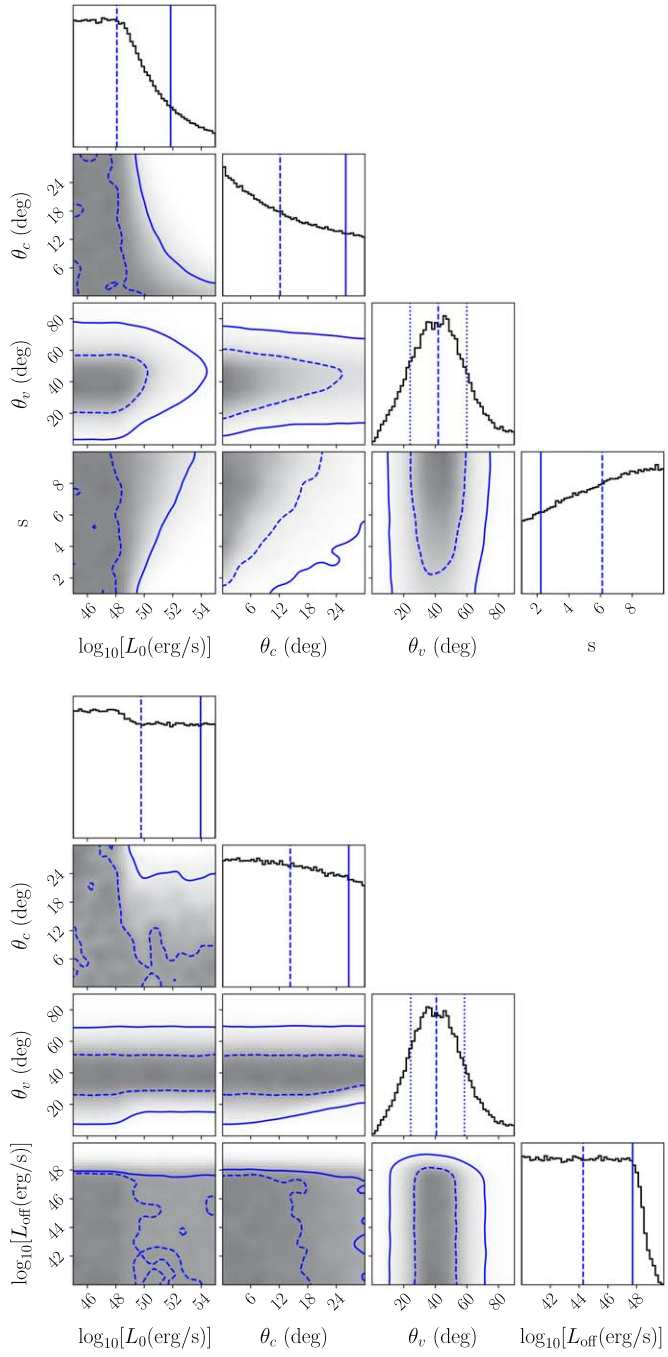

Figure 5. Same as Figure 2 but for a *power-law* model with s as a free parameter (top panel) and the *top-hat+isotropic* component (bottom panel). For the panel of the posterior distribution of s, the solid line reports the 10th percentile.

we report the 50% and 90% upper limits of $L(\theta_v)$, indicated with a dashed and solid line, respectively. As it can be noticed from this figure, apart from the *top-hat* structure, some values of L_0 and θ_c produce an unphysically bright $L(\theta_v)$ at large viewing angles. This effect is driven by the choice of the priors of L_0 and θ_c, which are not physically informed by any assumption about the maximum luminosity of a jet viewed strongly off-axis. In order to have such large luminosities off-axis, the jet should move relativistically not only along its axis but also along the line of sight, namely, outside the jet core. This is likely not physical, since it would by far exceed the energy budget of the jet, limited by the amount of mass accreted around the central engine. Therefore, for viewing angles $\theta_v \gg 10^\circ$ (typical opening angle of GRB jets), the upper limits on $L(\theta_v)$ shown in Figure 7 have to be taken with caution. However, we underline that, since we provide only upper limits on $L(\theta_v)$, our choice of the prior possibly overestimates the limits, making them more conservative and, therefore, not impacting the robustness of our conclusions.

A summary of all the properties of the posterior distributions are reported in Table 1. The table compares the percentiles of the priors and the posteriors of each parameter. For all the posteriors that show a decreasing trend, we report the upper limits as the 50th and 90th percentiles. In the case of the parameter s, since the posterior favors larger values, we report

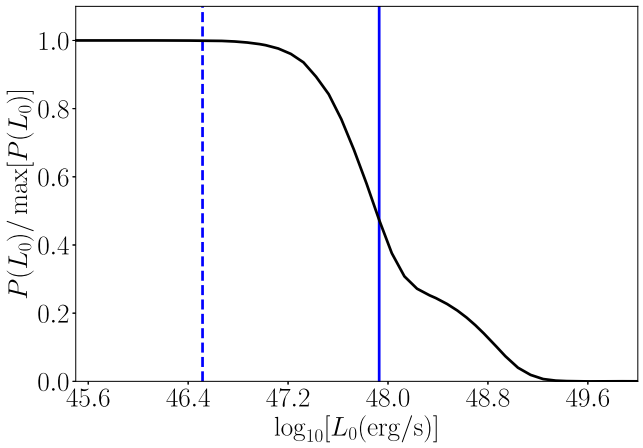

Figure 6. Posterior distribution of the apparent isotropic luminosity for the *isotropic* model. The solid and dashed vertical lines are the 90th and 50th percentiles of the distribution, respectively.

the lower limits as the 10th and 50th percentiles. The posterior of θ_v is well peaked as the prior, and we report the 1σ credible interval (16th and 84th percentiles) and the median value.

Since the GW merger considered in this work can potentially power a short GRB, it is useful to compare the constraints obtained here with the typical jet luminosities and opening angles collected in the literature. As a reference, we consider the short GRBs analyzed by Rouco Escorial et al. (2023). The authors combine observations of the prompt and afterglow phases of short GRBs, deriving the energetics of the jet and the opening angle of the jet from the detection of a jet break in the afterglow lightcurve. In particular, we consider the values of the isotropic equivalent energy $E_{\rm iso}$ and the opening angle θ_j reported in Table 4 of Rouco Escorial et al. (2023). In order to have an estimate of the isotropic equivalent luminosity, we compute $(1+z)E_{\rm iso}/t_{90}$, t_{90} being the timescale over which we receive 90% of the observed photons of the burst. Since the isotropic equivalent luminosity corresponds to the definition of our L_0 in the case of a *top-hat* jet, we compare in Figure 8 the $L_{\rm iso}$–θ_j values derived from Rouco Escorial et al. (2023) with the 2D posterior distribution of L_0–θ_c. We indicated with an arrow the GRBs for which we have only a lower limit of the opening angle θ_j. Comparing the 90% excluded region with the location of the $L_{\rm iso}$–θ_j points, we do not exclude that GW230529 produced a typical short GRB-like jet.

The value of the opening angle of the jet can be compared with the results of Sarin et al. (2022), where the authors combine the estimated rate of BNS and NSBH mergers with the rate of observed short GRBs, showing that the average opening angle of jets launched by NSBH mergers is in the range $15.^{\circ}3^{+3.0}_{-3.3}$ (1σ credibility), under the assumption of a top-hat jet structure. With the caveat that this range could be dependent on the assumptions on the NSBH population and the modeling of the jet emission, the authors find a value compatible with the exclusion regions derived in this work. Considering different EoSs, Zhu et al. (2024) estimate the amount of mass ejected by GW230529, including the fraction that goes into an accretion disk. Assuming a Blandford–Znajek jet with a Gaussian structure, they derive a probability of detecting a GRB-like emission of <5%, in line with the nondetection reported in this Letter.

Our analysis provides limits on the maximum on-axis isotropic luminosity and the jet opening angle. Therefore, it is possible to infer a limit on the beaming-corrected luminosity, defined as $L_b = L_0(1-\cos\theta_c)$. Since the GW analysis reports an upper limit on the amount of ejected mass, $M_{\rm ej} < 0.052\ M_\odot$, this also represents a limit on the maximum amount of mass bound to the central object that can potentially power the GRB jet. If we define η as the efficiency of conversion from the rest mass energy of the bound disk mass to the beaming-corrected energy of the jet, we can write

$$L_b = \eta \frac{M_{\rm acc} c^2}{t_{\rm acc}} = \eta \dot{M}_{\rm acc} c^2, \tag{28}$$

where $M_{\rm acc}$ is the fraction of the ejected mass that falls back and accretes around the central BH, while $t_{\rm acc}$ is the accretion timescale of the disk. Using the limits $L_0 \lesssim 10^{48}$ erg s^{-1} and $\theta_c \lesssim 15^{\circ}$ found for the *top-hat* structure, we derive a limit on η corresponding to

$$\eta \lesssim 1.9 \times 10^{-3} \left(\frac{M_{\rm acc}}{0.01 M_\odot}\right)^{-1} \left(\frac{t_{\rm acc}}{1\ \rm s}\right). \tag{29}$$

Since the conversion efficiency η cannot be larger than 1, we can exploit the upper limit on $M_{\rm ej}$ derived from the GW analysis to obtain a limit on the maximum allowed opening angle of the jet for a given value of L_0. Expressing $M_{\rm acc} = \epsilon M_{\rm ej}$ and including all our uncertainties in a parameter $\alpha = \epsilon/t_{\rm acc}$, we can impose that $\eta < 1$ and $M_{\rm ej} < 0.052\ M_\odot$, obtaining

$$\theta_c < \arccos\left(1 - \alpha \frac{0.052 M_\odot c^2}{L_0}\right). \tag{30}$$

In Figure 9, we report the regions of the L_0–θ_c plane that are not allowed by the condition $\eta < 1$ and $M_{\rm ej} < 0.052\ M_\odot$ for different values of α, overplotted to the 50% and 90% exclusion regions derived previously for the *top-hat* jet. The figure shows that the smaller the fraction of ejected mass that goes into an accretion disk, the larger the excluded region in the L_0–θ_c plane. The values of L_0–θ_c excluded by the condition $M_{\rm ej} < 0.052\ M_\odot$ are in agreement with the region excluded by our analysis, showing that the nondetection of γ-rays is compatible with the limited amount of ejected mass that can be channeled to power a GRB jet.

In order to infer more informative constraints on η, we consider the work performed by Chandra et al. (2024). The authors use a set of population synthesis models to derive the mass distribution of the two components of GW230529. In addition, adopting different EoSs, they estimate the mass of the remnant BH, as well as the amount of ejecta mass. The latter is calculated following the fitting formulae derived by Krüger & Foucart (2020) and Raaijmakers et al. (2021). Here we consider only the two EoSs, `H4` (Glendenning & Moszkowski 1991; Lackey et al. 2006; Read et al. 2009) and `DD2` (Hempel & Schaffner-Bielich 2010; Typel et al. 2010), that produce ejecta mass larger than 0. From the ejecta mass, for each EoS, we extract the posterior distribution of the bound disk mass. The final distribution of η is obtained by randomly extracting L_0 and θ_c from the *top-hat* posterior samples, combined with the distribution of the bound disk mass. The result is shown in Figure 10 for the two EoSs, `H4` and `DD2`, and assuming $t_{\rm acc} = 0.1$ s and $t_{\rm acc} = 1$ s, in the typical range expected for NSBH mergers (Ciolfi 2018). The 90% credibility posterior range is $\log_{10}\eta = -3.6^{+2.6}_{-2.4}$ ($\log_{10}\eta = -3.6^{+2.5}_{-2.3}$) for the `H4` EoS, and $t_{\rm acc} = 1$ s ($t_{\rm acc} = 0.1$ s), and $\log_{10}\eta = -4.4^{+3.2}_{-2.5}$ ($\log_{10}\eta = -4.3^{+3.1}_{-2.5}$) for the `DD2` EoS, and $t_{\rm acc} = 1$ s ($t_{\rm acc} = 0.1$ s).

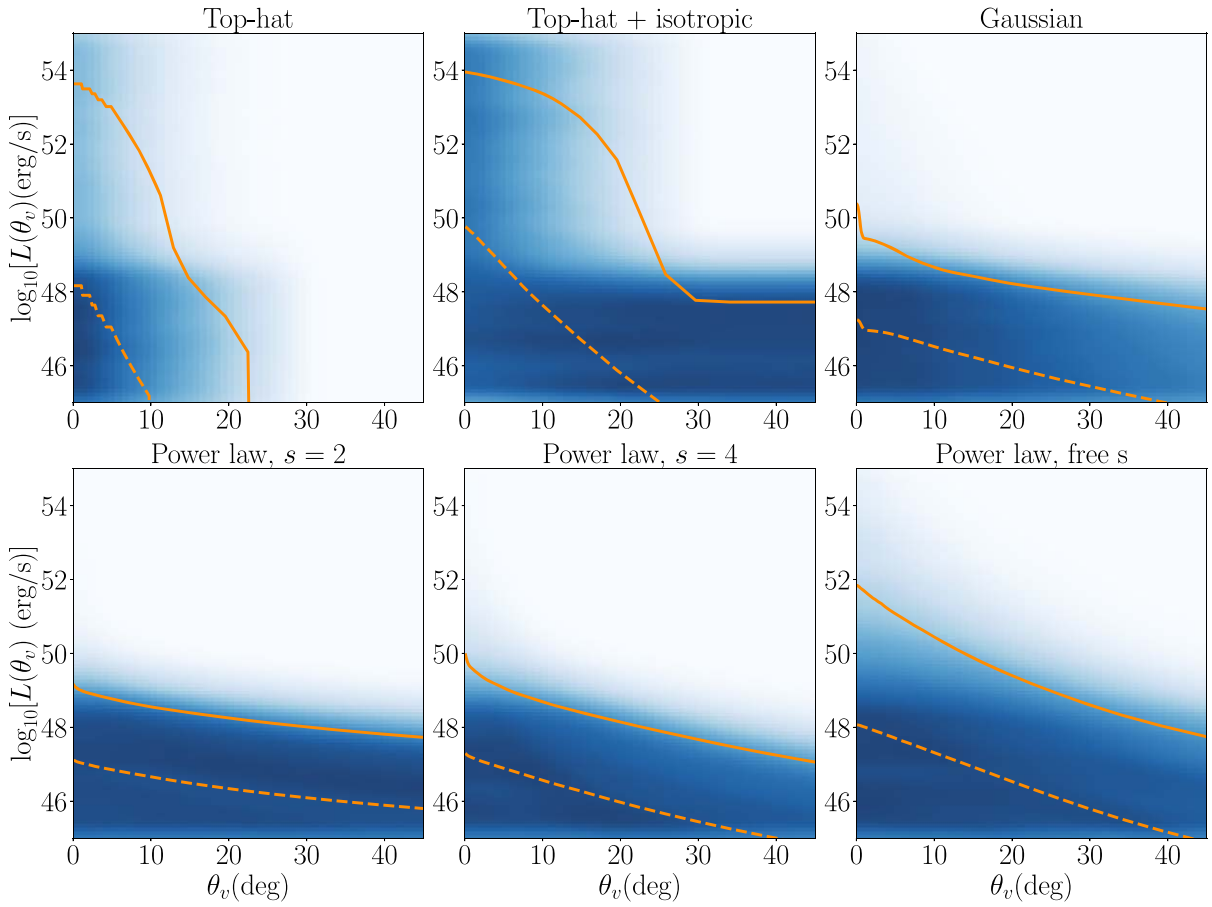

Figure 7. Posterior distribution of the luminosity profile $L(\theta_v)$, assuming different angular structures. The color density is produced by randomly extracting L_0, θ_c, s, and $L_{\rm off}$ from the relative posterior samples, which are then given as input to compute the luminosity profile $L(\theta_v)$ for each extraction. For each subplot, the solid (dashed) lines indicate the 90% (50%) upper limits.

9. Conclusions

GW230529 is the first NSBH candidate with a confirmed primary component in the lower mass gap. Being the NSBH event with the most symmetric mass ratio detected to date, this event is particularly promising for the production of EM emission in the form of a relativistic jet and/or a kilonova. No EM counterpart associated with this event has been reported so far (Sugita et al. 2023a, 2023b; IceCube Collaboration 2023; Karambelkar et al. 2023; Lesage et al. 2023; Longo et al. 2023; Savchenko et al. 2023; Waratkar et al. 2023). In the γ-ray domain, the combined presence of the Swift and Fermi telescopes ensured the full coverage of the sky at the time of the GW trigger. This enables us to derive the most stringent constraints on the possible GRB-like emission from the GW candidate. Combining the posterior distribution of sky position, luminosity distance, and inclination angle derived from the GW parameter estimation, we use the Swift-BAT and Fermi-GBM flux upper limits to derive the allowed values of the luminosity and opening angle of the putative jet. The analysis focused on multiple jet structures, including a top-hat, a Gaussian, a power law, as the inclusion of a possible isotropic component outside the jet core. The most conservative constraints are obtained for the *top-hat* configuration, for which there is a nonnegligible probability that the jet, even if bright, was strongly off-axis and, therefore, nondetectable. Considering the on-axis isotropic luminosity L_0 of a top-hat jet (in the rest-frame energy band 1 keV–10 MeV), we conclude that the nondetection of a γ-ray emission implies the absence of a jet with $L_0 \gtrsim 10^{48}$ erg s^{-1} and an opening angle $\gtrsim 15°$. These limits become stronger as soon as we admit the presence of an off-axis emission. Comparing the derived limits on the isotropic luminosity and opening angle with the typical values from short GRBs observed at cosmological distances, we cannot exclude that a system like GW230529 can potentially power a standard merger-driven GRB.

We emphasize that the ability to draw informative conclusions about the potential γ-ray emission of this compact binary merger (CBC) is largely due to the posterior distribution of the binary system's inclination angle derived from the GW analysis. Although the GW analysis does not provide stringent constraints on the viewing angle θ_v, it strongly disfavors large inclination angles. This is because CBCs tend to emit GWs preferentially in a direction perpendicular to the orbital plane. The anisotropic nature of GW emissions from CBCs significantly enhances the effectiveness of a combined GW +EM analysis, enabling modest constraints on the GRB jet structure.

The absence of EM counterparts to GW230529, as constrained by the joint Fermi–Swift search reported here, opens up the possibility that this event is a primordial BH merger (Huang et al. 2024), similar to that of GW190425 and GW190814 (Clesse & Garcia-Bellido 2022). In fact, there is no information from the GW analysis about the tidal deformability

Table 1
Limits on the Model Parameters, Comparing the Percentiles of the Prior and Posterior Distributions, for Different Jet Structures

Jet Structure	Prior			Posterior		
	L_0 (erg s^{-1})	θ_c (deg)	θ_v (deg)	L_0 (erg s^{-1})	θ_c (deg)	θ_v (deg)
Top-hat	10^{50} (10^{54})	15.1 (27.0)	$40.0^{+19.1}_{-18.2}$	3.4×10^{48} (4.7×10^{53})	11.3 (27.3)	$43.6^{+18.2}_{-19.1}$
Gaussian	10^{50} (10^{54})	15.1 (27.0)	$40.0^{+19.1}_{-18.2}$	2.1×10^{47} (2.3×10^{50})	12.5 (28.8)	$40.9^{+19.1}_{-18.2}$
Power law, $s = 2$	10^{50} (10^{54})	15.1 (27.0)	$40.0^{+19.1}_{-18.2}$	1.7×10^{47} (1.7×10^{49})	14.0 (28.5)	$40.9^{+18.2}_{-18.2}$
Power law, $s = 4$	10^{50} (10^{54})	15.1 (27.0)	$40.0^{+19.1}_{-18.2}$	2.7×10^{47} (1.1×10^{50})	12.5 (28.5)	$40.9^{+19.1}_{-18.2}$

Power Law, Free s

Prior				Posterior			
L_0 (erg s^{-1})	θ_c (deg)	θ_v (deg)	s …	L_0 (erg s^{-1})	θ_c (deg)	θ_v (deg)	s …
10^{50} (10^{54})	15.1 (27.0)	$40.0^{+19.1}_{-18.2}$	1.9 (5.5)	1.2×10^{48} (7.1×10^{51})	12.5 (26.0)	$41.8^{+18.1}_{-17.7}$	2.2 (6.1)

Top-hat+*Isotropic* Component

Prior				Posterior			
L_0 (erg s^{-1})	θ_c (deg)	θ_v (deg)	$L_{\rm off}$ (erg s^{-1})	L_0 (erg s^{-1})	θ_c (deg)	θ_v (deg)	$L_{\rm off}$ (erg s^{-1})
10^{50} (10^{54})	15.1 (27.0)	$40.0^{+19.1}_{-18.2}$	10^{45} (10^{49})	5.9×10^{49} (9.1×10^{53})	14.3 (26.6)	$40.7^{+17.7}_{-16.3}$	1.9×10^{44} (5.2×10^{47})

Note. We compare the percentiles of the prior and posterior distributions. The upper limits on L_0 and θ_c are reported as 50th (90th) percentiles. The credible interval of θ_v is at 1σ. Since the posterior $P(s)$ is monotonically increasing for larger values of s, we report lower limits as 10th (50th) percentiles.

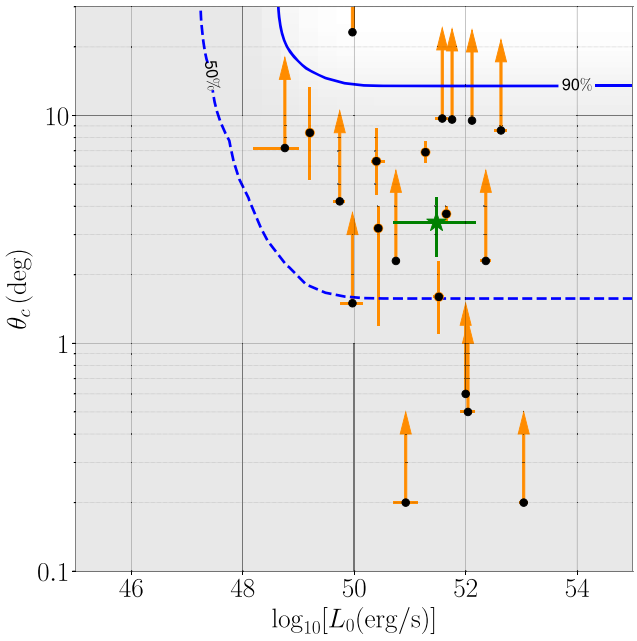

Figure 8. L_0–θ_c posterior probability (taken from the lower left panel of Figure 2) compared with estimates from Rouco Escorial et al. (2023) of isotropic luminosities and opening angles of a sample of short GRBs. The green point is relative to GW170817, for which the on-axis isotropic luminosity is taken from Salafia et al. (2019) and the opening angle from Ghirlanda et al. (2019). The solid and dashed lines are 90% and 50% exclusion regions derived from the present analysis under the assumption of a *top-hat* jet structure.

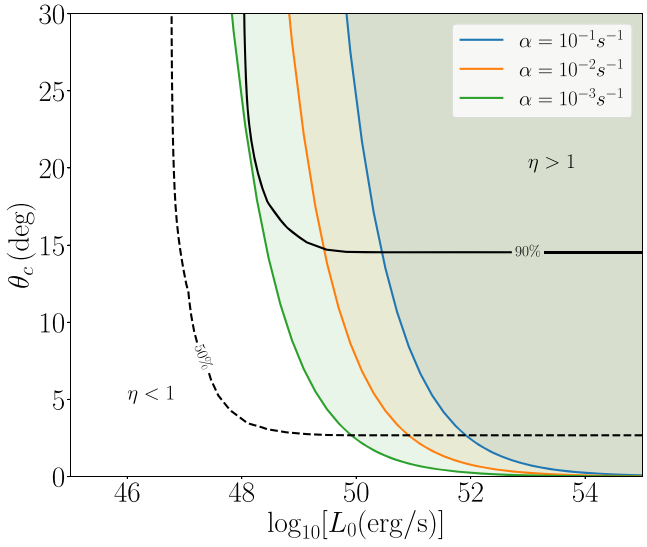

Figure 9. Regions of the L_0–θ_c plane excluded by the condition $M_{\rm ej} < 0.052\ M_\odot$. The exclusion lines are computed for different values of α, defined in the text. The dashed and solid black lines are the 50% and 90% exclusion regions reported from Figure 2.

of the secondary component. Therefore, the possibility that the secondary was a primordial BH cannot be totally excluded. The two component masses of GW230529 are in the mass gap around 2 $M_\odot$, where a peak is expected in the primordial BH (PBH) thermal model (Carr et al. 2021), and where no BHs from a confirmed astrophysical origin have been previously observed. The merger rates associated with these BBH events in the mass gap have large uncertainties but can be roughly estimated with the late binary formation in dense clusters of PBH through dynamical captures and are seen to be in agreement with observations (Clesse & Garcia-Bellido 2022).

In cases like GW230529, where the sky localization is very poorly constrained, systematic monitoring with ground-based

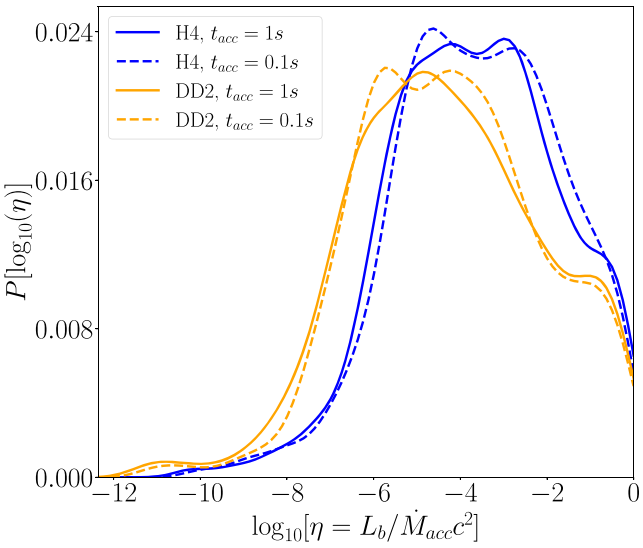

Figure 10. Posterior distribution of the efficiency factor η, which is the fraction of accretion power that is converted in the beaming-corrected luminosity of the jet. The posterior is produced for the EoSs `H4` and `DD2`, assuming an accretion timescale of 1 s and 0.1 s.

optical telescopes is unfeasible. Therefore, even if this system could power a potentially detectable kilonova emission, the lack of complete coverage of the GW sky region prevents us from inferring reliable limits on the brightness of this event in the optical/IR band.

On the other hand, this study demonstrates how crucial is the role of wide-field γ-ray/X-ray space telescopes, like Swift and Fermi, for the systematic coverage of the full sky at the moment of a GW merger. The exclusion of a high-energy EM signal can pose stringent constraints on the capability of NSBH mergers to successfully launch a relativistic jet. Moreover, since the GW sources detected by LVK are relatively close, we are also potentially sensitive to the off-axis γ-ray/X-ray emission, enabling us to shed more light on the structure of the relativistic outflows launched by these events. In the future, targeted searches performed jointly between Swift and Fermi will be of primary importance to detect the high-energy EM counterpart of GW mergers and, in the case of nondetection, pose the deepest limits on their intrinsic EM brightness in the γ-ray/hard X-ray domain.

Acknowledgments

The authors are grateful for computational resources provided by the LIGO Laboratory and supported by National Science Foundation grants PHY-0757058 and PHY-0823459. This material is based upon work supported by NSF's LIGO Laboratory, which is a major facility fully funded by the National Science Foundation. J.A.K. and J.D. acknowledge the support of NASA contract NAS5-0136. J.A.K., G.R., and S.R. acknowledge the support of NASA grant 80NSSC24K0488 through the Swift Guest Investigator program. J.A.K., G.R., and S.R. acknowledge the support of NASA grant 80NSSC24K0292 through the Fermi Guest Investigator program. The USRA coauthors gratefully acknowledge NASA funding through contract 80NSSC24M0035. The NASA authors gratefully acknowledge NASA funding through the Fermi-GBM project. The UAH coauthors gratefully acknowledge NASA funding from cooperative agreement 80MSFC22M0004. G.P. acknowledges the partial support by ICSC—Centro Nazionale di Ricerca in High Performance Computing, Big Data and Quantum Computing, funded by European Union—NextGenerationEU. K.C., I.G., R.K., and B.S. were supported by NFS awards AST_2307147, PHY_2308886, PHY_2309064, and PHY_2207638. ET acknowledges support from the European Research Council through the Consolidator grant BHianca (Grant agreement ID: 101002761) and the National Science Foundation (under award number 2108950).

Appendix
Note about the Apparent Luminosity Structure

Given a structure of the angular distribution of the energy released by the jet during the prompt emission, one can derive the observed flux received by the observer as a function of the viewing angle. Also, the typical duration of the burst $\delta t(\theta_v)$ depends on the viewing angle; therefore, one can define the angular structure of the luminosity per unit frequency as

$$L_\nu(\theta_v) = 4\pi D_L^2 \langle F_\nu(\theta_v)\rangle_{\delta t(\theta_v)}. \tag{A1}$$

Going from the flux density to the integrated flux in the 15–350 keV band, the apparent luminosity structure considered in this work corresponds to

$$L(\theta_v) = 4\pi D_L^2 k(D_L) \langle F_{15-350}(\theta_v)\rangle_{\delta t(\theta_v)}, \tag{A2}$$

being

$$F_{15-350}(\theta_v) = \int_{15\ \mathrm{keV}}^{350\ \mathrm{keV}} F_\nu(\theta_v) d\nu, \tag{A3}$$

where $k(D_L)$ is the k-correction. Therefore, the angular dependence of $L(\theta_v)$ is implicitly a combination of the angular dependence of the radiated energy per unit solid angle and the angular dependence of the spectrum, which typically softens as we move away from the jet axis.

Since the flux upper limits are derived by taking the maximum value over different spectral shapes, the derived upper limit on the luminosity has the advantage that it is valid for all the spectra considered, since it is the most conservative. This means that we do not have to make ad hoc assumptions about the angular dependence of the spectral shape. Therefore, the limits on $L(\theta_v)$ have to be interpreted as spectrum-independent. On the other hand, this also implies that, even if we can derive upper bounds on $L(\theta_v)$, these results are still degenerate with respect to the structure of the radiated energy $E(\Omega)$ and the angular dependence of the observed spectrum $S_\nu(\theta_v)$. Namely, given a constraint on $L(\theta_v)$, the corresponding constraint on $E(\Omega)$ still depends on $S_\nu(\theta_v)$, and vice versa. On the other hand, once models for $E(\Omega)$ and $S_\nu(\theta_v)$ are specified, an apparent luminosity structure $L(\theta_v)$ can be derived and directly compared with the constraints found in this Letter.

A.1. Upper Limit Maps

We show in Figure 11 the flux upper limit maps separately for Swift-BAT and Fermi-GBM. The upper limit is computed in the band 15–350 keV. The white region indicates the part of the sky occulted by the Earth.

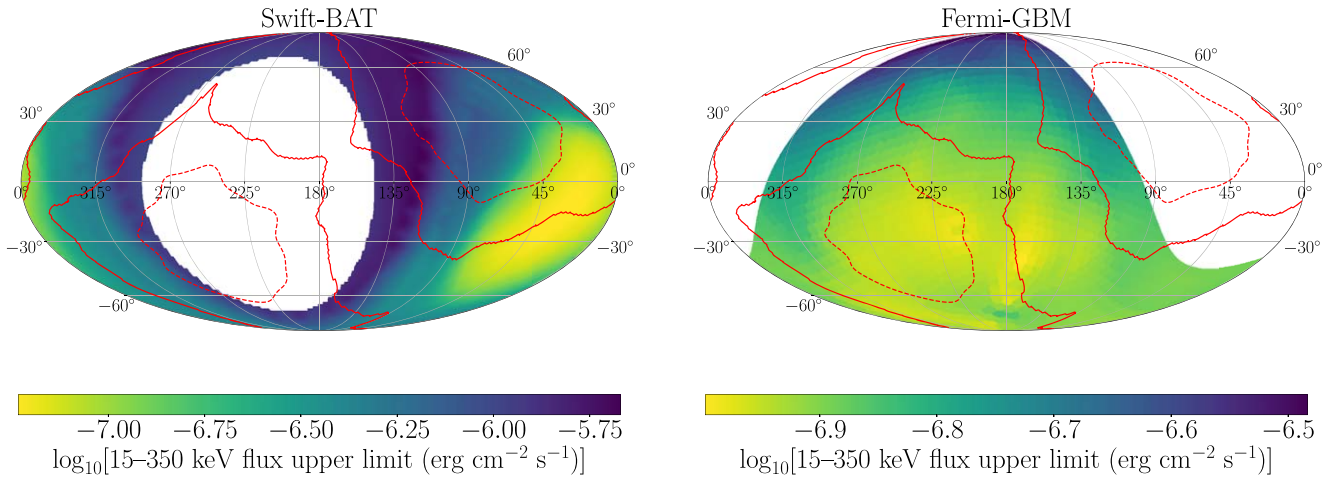

Figure 11. Upper-limit sky map in the 15–350 keV band for Swift-BAT (left) and Fermi-GBM (right). The upper limits are relative to a timescale of 1 s, computed at a 5σ confidence level. Solid and dashed lines are the GW contours at 90% and 50% credibility, respectively. The white region is the position of the Earth, for which no upper limits are available.

ORCID iDs

Samuele Ronchini https://orcid.org/0000-0003-0020-687X
Suman Bala https://orcid.org/0000-0002-6657-9022
Joshua Wood https://orcid.org/0000-0001-9012-2463
James Delaunay https://orcid.org/0000-0001-5229-1995
Simone Dichiara https://orcid.org/0000-0001-6849-1270
Jamie A. Kennea https://orcid.org/0000-0002-6745-4790
Tyler Parsotan https://orcid.org/0000-0002-4299-2517
Gayathri Raman https://orcid.org/0000-0003-0852-3685
Aaron Tohuvavohu https://orcid.org/0000-0002-2810-8764
Naresh Adhikari https://orcid.org/0000-0002-4559-8427
Narayana P. Bhat https://orcid.org/0000-0001-7916-2923
Sylvia Biscoveanu https://orcid.org/0000-0001-7616-7366
Elisabetta Bissaldi https://orcid.org/0000-0001-9935-8106
Eric Burns https://orcid.org/0000-0002-2942-3379
Sergio Campana https://orcid.org/0000-0001-6278-1576
Koustav Chandra https://orcid.org/0000-0003-4750-5551
William H. Cleveland https://orcid.org/0009-0003-3480-8251
Sarah Dalessi https://orcid.org/0000-0003-1835-570X
Juan García-Bellido https://orcid.org/0000-0002-9370-8360
Claudio Gasbarra https://orcid.org/0000-0001-8335-9614
Ish Gupta https://orcid.org/0000-0001-6932-8715
Dieter Hartmann https://orcid.org/0000-0002-8028-0991
Boyan A. Hristov https://orcid.org/0000-0001-9556-7576
Michelle C. Hui https://orcid.org/0000-0002-0468-6025
Rahul Kashyap https://orcid.org/0000-0002-5700-282X
Daniel Kocevski https://orcid.org/0000-0001-9201-4706
Bagrat Mailyan https://orcid.org/0000-0002-2531-3703
Hiroyuki Nakano https://orcid.org/0000-0001-7665-0796
Giacomo Principe https://orcid.org/0000-0003-0406-7387
Oliver J. Roberts https://orcid.org/0000-0002-7150-9061
Bangalore Sathyaprakash https://orcid.org/0000-0003-3845-7586
Lijing Shao https://orcid.org/0000-0002-1334-8853
Eleonora Troja https://orcid.org/0000-0002-1869-7817
Péter Veres https://orcid.org/0000-0002-2149-9846
Colleen A. Wilson-Hodge https://orcid.org/0000-0002-8585-0084

References

Abac, A. G., Abbott, R., Abouelfettouh, I., et al. 2024a, arXiv:2404.04248
Abac, A. G., Abbott, R., Abouelfettou, I., et al. 2024b, Observation of Gravitational Waves from the Coalescence of a 2.5-4.5 Msun Compact Object and a Neutron Star—Data Release, v1, Zenodo, doi:10.5281/zenodo.10845779
Abbott, B. P., Abbott, R., Abbott, T. D., et al. 2017, ApJL, 848, L12
Abbott, R., Abbott, T. D., Abraham, S., et al. 2020, ApJL, 896, L44
Abbott, R., Abbott, T. D., Abraham, S., et al. 2021a, PhRvX, 11, 021053
Abbott, R., Abbott, T. D., Abraham, S., et al. 2021b, ApJL, 915, L5
Abbott, R., Abbott, T. D., Acernese, F., et al. 2023, PhRvX, 13, 041039
Acernese, F., Agathos, M., Agatsuma, K., et al. 2015, CQGra, 32, 024001
Akmal, A., Pandharipande, V. R., & Ravenhall, D. G. 1998, PhRvC, 58, 1804
Akutsu, T., Ando, M., Arai, K., et al. 2021, PTEP, 2021, 05A101
Alexander, K. D., Schroeder, G., Paterson, K., et al. 2021, ApJ, 923, 66
Anand, S., Coughlin, M. W., Kasliwal, M. M., et al. 2021, NatAs, 5, 46
Band, D., Matteson, J., Ford, L., et al. 1993, ApJ, 413, 281
Barbieri, C., Salafia, O. S., Perego, A., Colpi, M., & Ghirlanda, G. 2020, EPJA, 56, 8
Barthelmy, S. D., Barbier, L. M., Cummings, J. R., et al. 2005, SSRv, 120, 143
Biscoveanu, S., Burns, E., Landry, P., & Vitale, S. 2023, RNAAS, 7, 136
Biscoveanu, S., Thrane, E., & Vitale, S. 2020, ApJ, 893, 38
Blackburn, L., Briggs, M. S., Camp, J., et al. 2015, ApJS, 217, 8
Burns, E. 2020, LRR, 23, 4
Carr, B., Clesse, S., García-Bellido, J., & Kühnel, F. 2021, PDU, 31, 100755
Chandra, K., Gupta, I., Gamba, R., et al. 2024, arXiv:2405.03841
Ciolfi, R. 2018, IJMPD, 27, 1842004
Clesse, S., & Garcia-Bellido, J. 2022, PDU, 38, 101111
Colombo, A., Duqué, R., Sharan Salafia, O., et al. 2024, A&A, 686, A265
DeLaunay, J., & Tohuvavohu, A. 2022, ApJ, 941, 169
Dichiara, S., Becerra, R. L., Chase, E. A., et al. 2021, ApJL, 923, L32
Dimple, M. K., & Arun, K. G. 2023, ApJL, 949, L22
Dobie, D., Stewart, A., Murphy, T., et al. 2019, ApJL, 887, L13
Escrivà, A., Kuhnel, F., & Tada, Y. 2022, arXiv:2211.05767
Farah, A., Essick, R., Doctor, Z., Fishbach, M., & Holz, D. E. 2020, ApJ, 895, 108
Fletcher, C., Wood, J., Hamburg, R., et al. 2024, ApJ, 964, 149
Fong, W., Berger, E., Margutti, R., & Zauderer, B. A. 2015, ApJ, 815, 102
Foreman-Mackey, D., Hogg, D. W., Lang, D., & Goodman, J. 2013, PASP, 125, 306
Foucart, F., Hinderer, T., & Nissanke, S. 2018, PhRvD, 98, 081501
Gehrels, N., Chincarini, G., Giommi, P., et al. 2004, ApJ, 611, 1005
Ghirlanda, G., Salafia, O. S., Paragi, Z., et al. 2019, Sci, 363, 968
Glendenning, N. K., & Moszkowski, S. A. 1991, PhRvL, 67, 2414
Goldstein, A., Hamburg, R., Wood, J., et al. 2019, arXiv:1903.12597
Gompertz, B. P., Levan, A. J., & Tanvir, N. R. 2020, ApJ, 895, 58
Gompertz, B. P., Nicholl, M., Smith, J. C., et al. 2023, MNRAS, 526, 4585
Gottlieb, O., Metzger, B. D., Quataert, E., et al. 2023, ApJL, 958, L33
Gottlieb, O., Nakar, E., & Piran, T. 2018, MNRAS, 473, 576
Graham, M. J., McKernan, B., Ford, K. E. S., et al. 2023, ApJ, 942, 99

Granot, J., & Kumar, P. 2003, ApJ, 591, 1086
Hamburg, R., Fletcher, C., Burns, E., et al. 2020, ApJ, 893, 100
Hamidani, H., & Ioka, K. 2023, MNRAS, 520, 1111
Hayes, F., Heng, I. S., Lamb, G., et al. 2023, ApJ, 954, 92
Hayes, F., Heng, I. S., Veitch, J., & Williams, D. 2020, ApJ, 891, 124
Hempel, M., & Schaffner-Bielich, J. 2010, NuPhA, 837, 210
Huang, Q.-G., Yuan, C., Chen, Z.-C., & Liu, L. 2024, arXiv:2404.05691
IceCube Collaboration 2023, GCN, 33980, 1
Karambelkar, V., Ahumada, T., Stein, R., et al. 2023, GCN, 33900, 1
Kawaguchi, K., Kyutoku, K., Nakano, H., et al. 2015, PhRvD, 92, 024014
Kilpatrick, C. D., Coulter, D. A., Arcavi, I., et al. 2021, ApJ, 923, 258
Krüger, C. J., & Foucart, F. 2020, PhRvD, 101, 103002
Kyutoku, K., Ioka, K., Okawa, H., Shibata, M., & Taniguchi, K. 2015, PhRvD, 92, 044028
Lackey, B. D., Nayyar, M., & Owen, B. J. 2006, PhRvD, 73, 024021
Lamb, G. P., & Kobayashi, S. 2017, MNRAS, 472, 4953
Lamb, G. P., Tanvir, N. R., Levan, A. J., et al. 2019, ApJ, 883, 48
Lazzati, D., Deich, A., Morsony, B. J., & Workman, J. C. 2017a, MNRAS, 471, 1652
Lazzati, D., López-Cámara, D., Cantiello, M., et al. 2017b, ApJL, 848, L6
Lesage, S. & Fermi-Gbm Team 2023, GCN, 33892, 1
Levan, A. J., Gompertz, B. P., Salafia, O. S., et al. 2024, Natur, 626, 737
LIGO Scientific Collaboration, Aasi, J., Abbott, B. P., et al. 2015, CQGra, 32, 074001
Longo, F., Tavani, M., Verrecchia, F., et al. 2023, GCN, 33894, 1
Martineau, T., Foucart, F., Scheel, M., et al. 2024, arXiv:2405.06819
Meegan, C., Lichti, G., Bhat, P. N., et al. 2009, ApJ, 702, 791
Mei, A., Banerjee, B., Oganesyan, G., et al. 2022, Natur, 612, 236
Metzger, B. D. 2019, LRR, 23, 1
Nakar, E., & Piran, T. 2017, ApJ, 834, 28
Ossokine, S., Buonanno, A., Marsat, S., et al. 2020, PhRvD, 102, 044055
Planck Collaboration, Aghanim, N., Akrami, Y., et al. 2020, A&A, 641, A6
Pratten, G., García-Quirós, C., Colleoni, M., et al. 2021, PhRvD, 103, 104056
Raaijmakers, G., Nissanke, S., Foucart, F., et al. 2021, ApJ, 922, 269
Ramirez-Ruiz, E., Celotti, A., & Rees, M. J. 2002, MNRAS, 337, 1349
Rastinejad, J. C., Gompertz, B. P., Levan, A. J., et al. 2022, Natur, 612, 223
Read, J. S., Lackey, B. D., Owen, B. J., & Friedman, J. L. 2009, PhRvD, 79, 124032
Rossi, E., Lazzati, D., & Rees, M. J. 2002, MNRAS, 332, 945
Rosswog, S. 2005, ApJ, 634, 1202
Rouco Escorial, A., Fong, W., Berger, E., et al. 2023, ApJ, 959, 13
Ryan, G., van Eerten, H., Piro, L., & Troja, E. 2020, ApJ, 896, 166
Salafia, O. S., & Ghirlanda, G. 2022, Galax, 10, 93
Salafia, O. S., Ghirlanda, G., Ascenzi, S., & Ghisellini, G. 2019, A&A, 628, A18
Sarin, N., Lasky, P. D., Vivanco, F. H., et al. 2022, PhRvD, 105, 083004
Savchenko, V., Ferrigno, C., Rodi, J., Coleiro, A., & Mereghetti, S. 2023, GCN, 33890, 1
Schutz, B. F. 2011, CQGra, 28, 125023
Sugita, S., Serino, M., Negoro, H., et al. 2023a, GCN, 33893, 1
Sugita, S., Yoshida, A., Sakamoto, T., et al. 2023b, GCN, 33897, 1
Tanaka, M., Hotokezaka, K., Kyutoku, K., et al. 2014, ApJ, 780, 31
Thakur, A. L., Dichiara, S., Troja, E., et al. 2020, MNRAS, 499, 3868
Tohuvavohu, A., Kennea, J. A., DeLaunay, J., et al. 2020, ApJ, 900, 35
Troja, E., Fryer, C. L., O'Connor, B., et al. 2022, Natur, 612, 228
Troja, E., King, A. R., O'Brien, P. T., Lyons, N., & Cusumano, G. 2008, MNRAS, 385, L10
Troja, E., Piro, L., Ryan, G., et al. 2018, MNRAS, 478, L18
Troja, E., Piro, L., van Eerten, H., et al. 2017, Natur, 551, 71
Troja, E., Sakamoto, T., Cenko, S. B., et al. 2016, ApJ, 827, 102
Troja, E., van Eerten, H., Ryan, G., et al. 2019, MNRAS, 489, 1919
Typel, S., Röpke, G., Klähn, T., Blaschke, D., & Wolter, H. H. 2010, PhRvC, 81, 015803
von Kienlin, A., Meegan, C. A., Paciesas, W. S., et al. 2020, ApJ, 893, 46
Waratkar, G., Bhalerao, V., Bhattacharya, D., et al. 2023, GCN, 33896, 1
Watson, A. M., Butler, N. R., Lee, W. H., et al. 2020, MNRAS, 492, 5916
Yang, J., Ai, S., Zhang, B.-B., et al. 2022, Natur, 612, 232
Yang, Y.-H., Troja, E., O'Connor, B., et al. 2024, Natur, 626, 742
Zhu, J.-P., Hu, R.-C., Kang, Y., et al. 2024, arXiv:2404.10596
Zhu, J.-P., Qin, Y., Wang, Z.-H.-T., et al. 2024, MNRAS, 529, 4554
Zhu, J.-P., Wang, X. I., Sun, H., et al. 2022, ApJL, 936, L10
Zhu, J.-P., Wu, S., Yang, Y.-P., et al. 2021, ApJ, 921, 156